fire

MDPI

Article

Bond Behaviour of Grouted Strands at Elevated Temperatures Considering Tendon Eccentricity

Xiqiang Wu [1], Chenhao Ru [1], Ting Huang [2], Wen Xiong [3,*] and Francis Tat Kwong Au [4]

[1] Department of Intelligent Low-Altitude & Spatial Informatics, School of Transportation, Southeast University, Nanjing 210018, China; wuxiqiang@seu.edu.cn (X.W.); 220243577@seu.edu.cn (C.R.)
[2] School of Civil Engineering, Guilin University of Technology, Guilin 541004, China; tingingh@glut.edu.cn
[3] Department of Bridge Engineering, School of Transportation, Southeast University, Nanjing 210018, China
[4] Department of Civil Engineering, The University of Hong Kong, Hong Kong, China; francis.au@hku.hk
* Correspondence: wxiong@seu.edu.cn

Abstract

Tendon eccentricity produces non-uniform grout thickness within ducts in bonded post-tensioned concrete structures. Its implications for bond behaviour were investigated through 53 pull-out tests on mono- and triple-strand tendons embedded in grouted corrugated steel ducts within concrete cylinders. Eccentricity was varied at ambient temperature, whereas tests during heating and after cooling used the maximum eccentricity for each tendon configuration. The programme covered 20–600 °C and included comparisons of water cooling for mono-strand specimens and helical confinement for triple-strand specimens. Increasing eccentricity reduced ambient-temperature bond strength. Bond strength and initial stiffness decreased with temperature, with the fitted relationships indicating reductions to half their ambient-temperature values at approximately 242 °C and 118 °C, respectively. Bond strength recovered slightly after cooling, and water- and air-cooled mono-strand specimens showed similar responses under the tested conditions. For specimens classified as having medium confinement, post-peak residual bond strength averaged approximately 70% of the corresponding characteristic bond strength, while specimens exhibiting through splitting retained little residual resistance. Helical reinforcement improved the post-peak response of triple-strand tendons, although its contribution to bond strength was limited at 100–300 °C when concrete cover spalling occurred. The results were used to recalibrate a trilinear bond–slip model for the observed confinement conditions.

Keywords: grouted tendons; bond–slip behaviour; tendon eccentricity; elevated temperatures; cooling; confinement

Check for updates

Academic Editor: Hugo Rodrigues

Received: 19 September 2026
Revised: 22 October 2026
Accepted: 27 October 2026
Published: 28 October 2026

Copyright: © 2026 by the authors. Licensee MDPI, Basel, Switzerland. This article is an open access article distributed under the terms and conditions of the Creative Commons Attribution (CC BY) license.

1. Introduction

Bonds between prestressing tendons and cement grout enable force transfer within bonded post-tensioned concrete members. During fire exposure, deterioration of this interaction can affect tendon slip and structural response in addition to the changes in the mechanical properties of the constituent materials. Research on the fire performance of prestressed concrete members has, therefore, identified bond behaviour as an important consideration in structural assessment [1]. Numerical investigations of strand–concrete interaction also underline the need to represent bond deterioration in fire analysis [2]. For grouted tendons, this requires an understanding of both the response during heating and the bond resistance remaining after cooling.

The geometry of a strand and the restraint supplied by its surroundings are central to interpreting its bond behaviour. Early experimental investigations provided a basis for characterising the bond of prestressing strands [3]. More recent work has examined geometric features that are difficult to represent using models developed for reinforcing bars. Dai et al. [4] constructed a three-dimensional meso-scale model incorporating the helical geometry of strands and investigated the influence of strand eccentricity, among other parameters, on strand–concrete interaction. For post-tensioning strands embedded in grouted metal ducts, Ferretti et al. [5] showed that grouting defects reduced bond stresses and altered the bond–slip response. These studies address different aspects of the surrounding material and interface geometry. Their findings motivate closer examination of tendon position within a duct but do not directly describe the response of an eccentrically grouted tendon during heating and subsequent cooling. Recent studies of reinforcing bars have clarified how specimen geometry and confinement affect bond after thermal exposure. Asghari Ghajari and Yousefpour [6] used modified beam-end specimens to investigate residual bond behaviour for different bar diameters, concrete strengths and transverse reinforcement ratios. Das et al. [7] examined the effects of bonded length and bar position under different fire-exposure configurations, drawing attention to the influence of thermal gradients and cracking. Bošnjak et al. [8] further investigated concrete cover and transverse reinforcement in relation to residual bond performance. Liu et al. [9] systematically studied the effects of lateral confinement on bond behaviour and failure modes at steel bar–grout interfaces, and they [10] further investigated the effects of bar embedment length and loading rate on bond performance after thermal exposure. At the material level, Xiao et al. [11] characterised the strain-rate-dependent compressive response of high-strength concrete after heating, and the comprehensive review [12] synthesised evidence on high-performance concrete at elevated temperatures, including the mechanisms and influencing factors of thermal spalling. Collectively, these studies show that the temperature alone is insufficient to characterise bond response, the surrounding material, restraint conditions, reinforcement location, loading rate and thermally induced damage also need to be considered.

Cooling and testing procedures introduce further differences between reported bond responses. Liu et al. [13] investigated corroded reinforcement subjected to different cooling methods and reported lower bond strength after water cooling than after natural cooling. The presence of corrosion limits direct application of that finding to uncorroded grouted tendons. Abuhishmeh et al. [14] assessed bonding after high-temperature exposure using both pull-out and beam-end tests on high-strength reinforcing bars, illustrating the relevance of the test configuration when interpreting thermal degradation. Comparisons of bond performance consequently need to distinguish specimens loaded while hot from those loaded after cooling, while retaining the relevant material and restraint conditions. Evidence concerning reinforcement position is also available for grout without external confinement. Peng et al. [15] examined steel bars at the centre, side and corner of grout specimens after elevated-temperature exposure and reported differences in bond capacity and failure mode. Li et al. [16] developed a model for the residual bond of steel bars in concrete that accounts for radial restraint and cracking of the concrete cover. These studies provide a basis for considering non-uniform surrounding material and resistance to splitting. Application to grouted strand tendons nevertheless requires attention to the helical wire geometry, the arrangement of adjacent strands, and the restraint supplied by the duct and outer concrete.

Our previous study [17] investigated mono-, triple- and quadruple-strand tendons positioned centrally in grouted ducts at temperatures of 20–600 °C, including tests performed while hot and after air cooling. However, in practice, curvature of the tendon profile can position strands towards one side of a duct, resulting in non-uniform grout

thickness. The previous programme did not examine this eccentric arrangement, water cooling or additional helical confinement. Its results, therefore, provide a reference for the present investigation but do not establish whether the same failure patterns and model parameters apply under these additional conditions.

The present study extended this experimental basis through 53 pull-out tests on mono- and triple-strand tendons in grouted corrugated steel ducts embedded in concrete cylinders. Tendon eccentricity was first varied at ambient temperature. Subsequent tests used the maximum eccentricity for each tendon configuration and covered loading at elevated temperatures up to 600 °C and after air cooling. For mono-strand specimens, the maximum eccentricity was 16.4 mm, corresponding to the strand just contacting the inner wall of the duct. Additional series examined water cooling for mono-strand specimens and helical confinement for triple-strand specimens. The programme evaluated failure modes, initial bond stiffness, characteristic bond strength and post-peak resistance to distinguish the ambient-temperature eccentricity effect from the thermal response at maximum eccentricity. Compared with the previous study [17], the current study investigates the reduction in bond capacity associated with eccentricity, the sensitivity of post-heating bond behaviour to cooling method, and the effectiveness of additional confinement in maintaining post-peak resistance in eccentric tendon arrangements. These results were used to recalibrate the existing trilinear framework for the confinement conditions observed in the present tests.

2. Experimental Programme

The experimental programme combined ambient-temperature tests at different tendon eccentricities with tests at elevated temperatures and after cooling. The pull-out arrangement followed the general approach used in our earlier study of centred grouted tendons [17], with specimen geometry and thermal conditions specified for the present programme. The design also drew on recommendations for ambient-temperature pull-out testing [18,19].

2.1. Specimen Geometry

Each specimen comprised a prestressing tendon, cement grout, a corrugated steel duct and a surrounding concrete cylinder (Figure 1). The cylinder was 240 mm long and 150 mm in diameter, dimensions limited by the furnace chamber. Bonding was restricted to an 80 mm length near the middle of the specimen to facilitate relatively uniform heating of the strand–grout interface, meaning that the bonded length was 80 mm. The nominal diameter d_b of the seven-wire strand was 15.2 mm; thus, the cylinder diameter and bonded length l_b were approximately $10d_b$ and $5d_b$, respectively. The cylinder diameter lay within the 82–172 mm range reported for bond tests [20], and the bonded-length ratio followed that adopted by Diederichs and Schneider [21]. PVC tubes with an internal diameter slightly greater than the tendon size prevented bonding at both ends. The duct diameter was 50 mm. Where additional confinement was provided, a steel helix was arranged concentrically with the concrete cylinder. Tendon eccentricity is the distance between the duct centre and the tendon centroid, as illustrated in Figure 1b. For the triple-strand arrangement, the centroid was taken as the centre of threefold rotational symmetry of the assumed cross-section. The mono-strand eccentricities were 0, 4.8, 8.8, 12.8 and 16.4 mm; the triple-strand eccentricities were 0, 4.6 and 8.6 mm. The maximum values of 16.4 mm and 8.6 mm corresponded to contact between the tendon and the duct inner wall, accounting for the effective internal duct geometry. Eccentricity was varied in the ambient-temperature tests, whereas all tests involving heating used the maximum eccentricity for the relevant tendon configuration. These positions were obtained by moving the duct while retaining a common axis for the tendon and concrete cylinder.

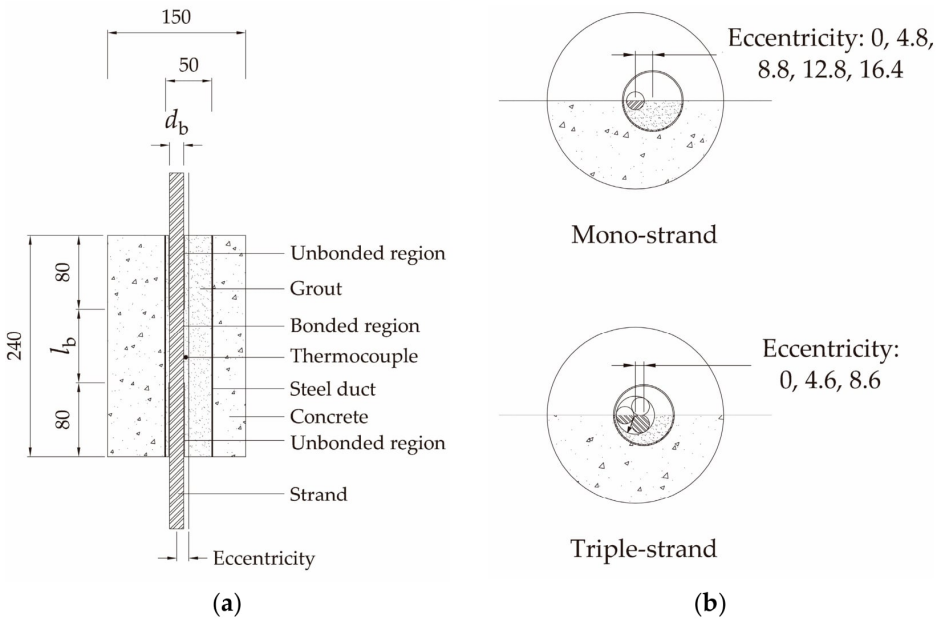

Figure 1. Test specimen (unit: mm): (**a**) vertical cross-section for mono-strand tendon, (**b**) horizontal cross-sections.

2.2. Materials and Specimen Fabrication

The grout was made with Grade 52.5R ordinary Portland cement at a water–cement ratio of 0.4, within the 0.35–0.45 range commonly adopted in engineering practice to provide suitable workability and fluidity. The concrete had a design cylinder strength of 50 MPa and the mix proportions listed in Table 1. The granitic coarse and fine aggregates had sizes of 20 mm and 10 mm, respectively. For compressive-strength quality control, each test series included three grout cylinders, 100 mm in diameter and 200 mm high, and three concrete cylinders, 150 mm in diameter and 300 mm high. The low-relaxation seven-wire strands conformed to BS 5896 [22] and had a nominal diameter of 15.2 mm, an ambient-temperature Young's modulus of 200 GPa and an ultimate tensile strength of 1860 MPa [23]. The tested strength of the grout, concrete and strand tendons is given in Appendix A.1 in Appendix A. Additional confinement, where specified, consisted of 6 mm steel wire formed into a helix with an 86 mm coil diameter and a 10 mm pitch. The helix extended throughout the concrete cylinder and shared its centreline.

Table 1. Mix proportions of concrete.

Material	Mix (kg/m^3)
Cement	487.1
Coarse aggregate	681.3
Fine aggregate	832.7
Water	249.5

A 1 mm diameter chromel–alumel thermocouple was installed in the bonded region to monitor its temperature. The specimens were fabricated by injecting grout into the duct, allowing it to cure for 7 days, and then casting the surrounding concrete (Figure 2). After concreting, the specimens were cured in indoor air and were approximately four months old at the start of heating or, for the ambient-temperature series, at loading.



(**a**) (**b**)

Figure 2. Fabrication of specimens: (**a**) before grout injection, (**b**) before concreting.

2.3. Heating Procedure

2.3.1. Heat-Transfer Analysis for Selection of the Heating Rate

Heating was carried out in an electric furnace with a maximum operating temperature of 1400 °C. The furnace programme was selected with reference to the temperature history at the tendon location. Relevant considerations included the heating rates of 1–20 °C/min discussed in the literature [20], approximately isothermal conditions in the bonded region [21,24,25], and completion of a test within one day [21,25]. Heating duration and heating history may also affect bond deterioration [26,27]. Abaqus heat-transfer analyses of a reference slab and a pull-out specimen (Figure 3) were, therefore, used to inform the furnace programme, with the reference slab subjected to the ISO 834 standard temperature–time curve [28].

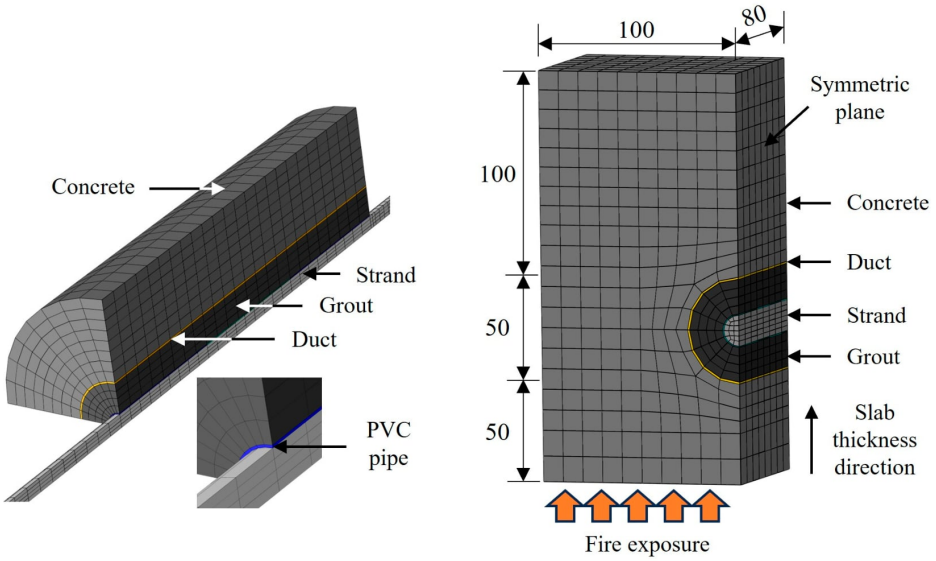

(**a**) (**b**)

Figure 3. Heat-transfer models: (**a**) pull-out specimen, (**b**) grouted strand in the reference slab (unit: mm).

The reference pull-out model comprised concrete, grout, a steel duct, an equivalent solid tendon and PVC sleeves at the unbonded ends. A quarter of the centred cylindrical configuration was modelled, with a concrete radius of 75 mm, a length of 240 mm, a tendon diameter of 15.2 mm and an 80 mm central bonded region. Eight-node linear heat-transfer brick elements (DC3D8) were used. The tendon–grout interface in the bonded region was

tied, and thermal contact was specified at the sleeve interfaces. Figure 3a shows the pull-out model, and Figure 3b shows the reference slab model. The centred pull-out model served as the thermal reference for selecting the furnace programme.

The thermal properties of concrete and steel were based on Eurocode provisions [29,30], with conductivity and specific heat defined as functions of temperature only. The same temperature-dependent conductivity and specific-heat descriptions were assigned to the concrete, grout and interfacial bond region. The duct and tendon shared the same steel thermal properties. Constant densities of 2400, 1850 and 7800 kg/m^3 were assigned to concrete, grout/the bond region and steel, respectively. The PVC sleeves were assigned a conductivity of 0.19 W/(m·K), a density of 1400 kg/m^3 and a specific heat of 1170 J/(kg·K). Convective and radiative heat exchange was applied to the furnace-exposed surfaces, using a convection coefficient of 25 W/(m^2·K) and an emissivity of 0.8. Surfaces exposed to the ambient environment exchanged heat with surroundings at 20 °C, using a convection coefficient of 9 W/(m^2·K) and the same emissivity.

Figure 4a compares the simulated bonded-region temperature histories for furnace heating rates of 1, 1.5, 3 and 5 °C/min with the reference slab history at a depth of 75 mm. The 1.5 °C/min programme provided a gradual rise in bonded-region temperature and was selected as a practical approximation to the slab response. The agreement varied over the heating period, so this selection does not imply that the complete slab history is reproduced or that this rate is the closest match at every temperature. A furnace heating rate of 1.5 °C/min was adopted for the tests.

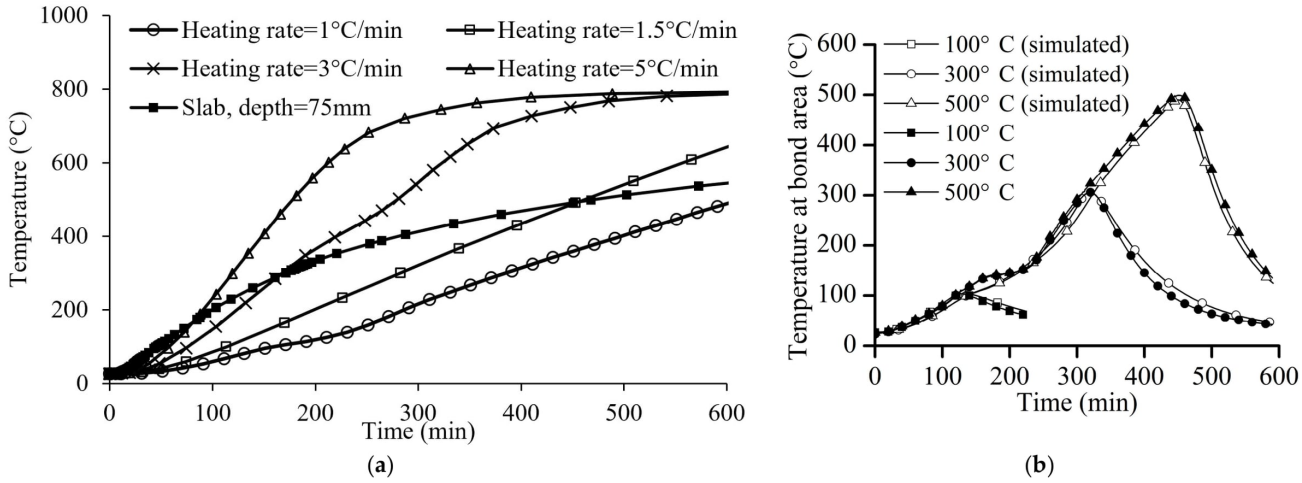

Figure 4. Temperature histories: (**a**) comparison of furnace heating rates for the pull-out specimen with the reference slab response at a depth of 75 mm; (**b**) simulated and measured bonded-region temperatures for target temperatures of 100, 300 and 500 °C.

Figure 4b compares simulated bonded-region temperatures with measurements from the actual pull-out tests at target temperatures of 100, 300 and 500 °C. The model captured the main heating and cooling trends in these comparisons, supporting its use to describe the thermal histories of the cases examined. During the critical loading interval of approximately 3 min, spanning attainment of the maximum bond strength and the immediately subsequent response, the prescribed furnace temperature increased by approximately 4.5 °C, and the reported change at the strand–grout interface remained within 2 °C. This limited local temperature change supported treating the bonded region as approximately constant local temperature during the critical loading interval.

2.3.2. Heating and Cooling Procedures

The target bonded-region temperatures were 20 °C for the ambient tests and 100, 200, 300, 400, 500 and 600 °C for the heated series. For testing while hot, loading started shortly before the measured temperature reached the target because the bonded-region temperature continued to rise during loading. The critical loading stage, covering the attainment of and progression beyond the maximum bond strength, lasted approximately 3 min. During this stage, the difference between the measured bonded-region temperature and the target remained below 5 °C. This interval did not represent the total duration of the pull-out test. For tests after cooling, the furnace was opened before the bonded-region thermocouple reached the preset temperature, allowing for the subsequent internal temperature rise so that the maximum temperature remained close to the target. Separate specimens were cooled either in air or by continuous water spraying. In the water-cooled series, spraying continued until the thermocouple in the bonded region recorded room temperature, after which the specimen was subjected to the pull-out test. The spraying duration was, thus, determined by the measured temperature rather than a prescribed fixed time.

2.4. Pull-Out Testing

Table 2 summarises all 53 specimens. Series 1 comprised 16 ambient-temperature specimens: 10 mono-strand specimens and 6 triple-strand specimens, with two tests at each eccentricity. Series 2 comprised 12 mono-strand specimens, with 1 specimen tested while hot and 1 after air cooling at each of the six target temperatures. Series 3 followed the same arrangement for 12 triple-strand specimens. Series 4 comprised six mono-strand specimens, one tested after water cooling from each target temperature. Series 5 comprised seven triple-strand specimens with helical reinforcement: one tested at ambient temperature and one tested while hot at each of the six target temperatures. The six elevated target temperatures in Series 2–5 were 100, 200, 300, 400, 500 and 600 °C. These series used maximum eccentricities of 16.4 mm for mono-strand tendons and 8.6 mm for triple-strand tendons. Each specimen was subjected to one pull-out test; no additional specimens were included outside the 53-specimen programme.

Table 2. Parameters in each test series.

Test Series	No. of Specimens	No. of Strands	Tendon Eccentricity	Additional Helical Reinforcement	Thermal Conditions
1	10	1	Varies	No	Ambient
	6	3	Varies	No	Ambient
2	12	1	Max.	No	Elevated; air-cooled
3	12	3	Max.	No	Elevated; air-cooled
4	6	1	Max.	No	Water-cooled
5	7	3	Max.	Yes	Ambient (1); elevated (6)

The loading assembly operated through the furnace and comprised a hydraulic jack, two drawbars, a reaction frame, a tendon anchor and steel plates (Figure 5). Two insulating firebricks and a bearing cylinder formed part of the specimen support arrangement. Instrumentation comprised a load cell, a linear variable differential transformer (LVDT) for measuring free-end slip, and thermocouples positioned adjacent to the specimen surface, in addition to the thermocouple in the bonded region.

Ambient-temperature test recommendations propose a rubber or polychloroprene layer at the specimen–bearing-cylinder contact to reduce lateral restraint [18,19]. As these

materials were unsuitable for the present heating conditions, the contact surfaces were smoothed before each test. A single-hole or three-hole anchor gripped the loaded end of the tendon. Clearance between the anchor and the top of the concrete cylinder allowed the three strands to spread towards the anchor holes.

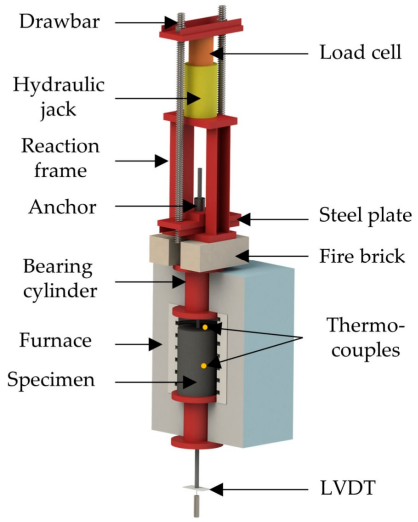

Figure 5. Test setup.

No initial prestress was applied to the strands. During pull-out loading, the anchor was pulled upwards while the bearing cylinder restrained the upper surface of the specimen. The mean displacement rate was 2.6 mm/min, within the ASTM range of 2.5 ± 0.13 mm/min [18]. Load, free-end slip and temperature were recorded with resolutions of 0.1 kN, 0.01 mm and 0.1 °C, respectively. The LVDT measured free-end slip, without correction for apparatus deformation or strand elongation. Loading was terminated when the measured slip exceeded the 20 mm range of the LVDT.

2.5. Evaluation of Bond Stress

Bond stress was evaluated using the tendon-envelope approach adopted in the previous study [17]. The idealisation assumes that progressive detachment of grout between adjacent wires or strands can produce a failure surface approximating the envelope illustrated in Figure 6. This idealisation assigns a uniform equivalent bond stress t_b over the bonded length, giving the following relation between bond stress and pull-out force P:

$$t_b = P/(l_e \cdot l_b), \quad (1)$$

where l_e is the envelope perimeter, equal to πd_b for a mono-strand tendon and $(\pi + 3)d_b$ for a triple-strand tendon, and l_b is the bonded length. For eccentric tendons, this equivalent stress describes the overall force transfer. It does not imply a uniform local interfacial stress distribution.

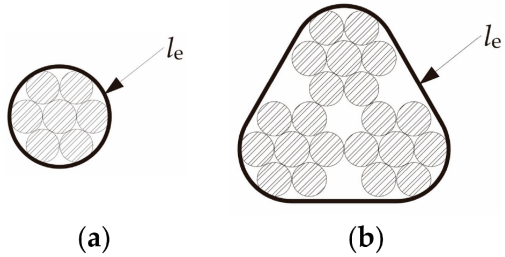

Figure 6. Envelope perimeter of tendon: (**a**) mono-strand; (**b**) triple-strand.

3. Test Results and Discussion

3.1. Failure Modes

The furnace enclosure prevented direct observation of crack development during loading. Failure modes were, therefore, identified from the specimens after testing, and the condition of the steel duct was examined by cutting the specimens into sections.

Pull-out failure is generally associated with strong confinement and a short bonded length, whereas splitting is relevant to many practical anchorage conditions [31] and becomes more likely at elevated temperatures [24]. Only splitting failures were identified in the present programme. Partial splitting left a few cracks in the concrete and an intact duct; through splitting broke the concrete into pieces and fractured the duct (Figure 7). Triple-strand specimens without additional helical reinforcement exhibited through splitting when tested while hot at, or after cooling from, temperatures not exceeding 300 °C. This classification excludes the helically reinforced specimens. The remaining specimens exhibited partial splitting.



(**a**) (**b**)

Figure 7. Typical failure modes: (**a**) partial splitting; (**b**) through splitting.

3.2. Effect of Tendon Eccentricity

At ambient temperature, increasing eccentricity reduced bond strength for both tendon configurations, while the overall shape of the bond–slip curves changed little, as illustrated in Figure 8, in which each curve comprised an ascending branch and a descending branch. A possible explanation is that the non-uniform grout thickness produces an uneven distribution of interfacial stress, although the reported measurements did not resolve that distribution. Moving the duct changes the grout thickness, as illustrated in Appendix A.2. The grout thickness on the side nearest the duct wall is reduced, which changes local restraint and force transfer. The uneven interfacial stress may then result in local cracking before the resistance at the interface is developed. The strength reduction matters for bonded post-tensioned members, in which tendon curvature can place strands close to the duct wall: using values measured for centred tendons could overestimate the available bond resistance. The subsequent heated series, therefore, focused on the maximum eccentricity for each tendon configuration. These series characterised that limiting position rather than providing a complete eccentricity–temperature relationship. As shown in Figure 8, the mono- and triple-strand specimens exhibit different initial tangent slopes in their bond–slip curves. These slopes represent the apparent bond stiffness in the small-slip regime, which may arise from variations in load-transfer geometry and strand–grout contact conditions between the two configurations, which influence the mobilisation of bond resistance during the initial stage of loading.

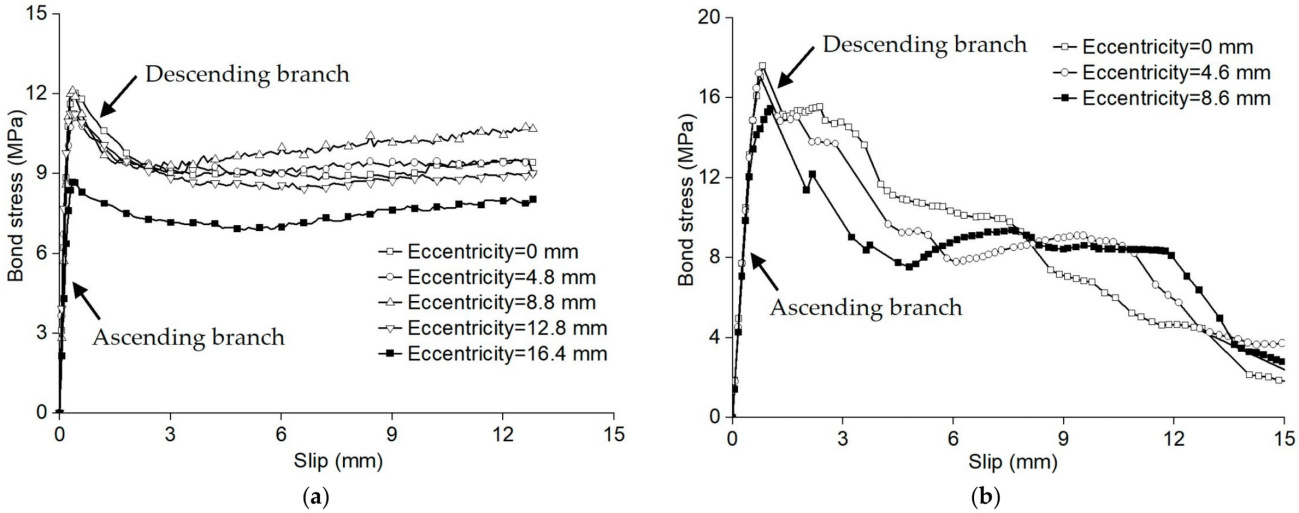

Figure 8. Bond–slip curves for different eccentricities at ambient temperature: (**a**) mono-strand; (**b**) triple-strand.

3.3. Bond–Slip Responses of Mono- and Triple-Strand Tendons

Figures 9 and 10 compare the mono- and triple-strand responses, respectively, during heating and after air cooling. Temperature substantially changed the bond–slip response, consistent with thermal deterioration of the grout, concrete and steel duct. Grout transfers force from the helical strand surface to the surrounding duct. Dehydration and thermal cracking can weaken the grout supporting this contact, so a given slip produces less resistance. Cracking in the outer concrete reduces restraint against lateral deformation of the grouted duct. A reduction in the stiffness and strength of the steel duct also reduces its resistance to this deformation. These changes can reduce contact pressure and the support needed for friction and mechanical interlocking to develop. The remaining contact and duct restraint can still transfer force as slip increases.

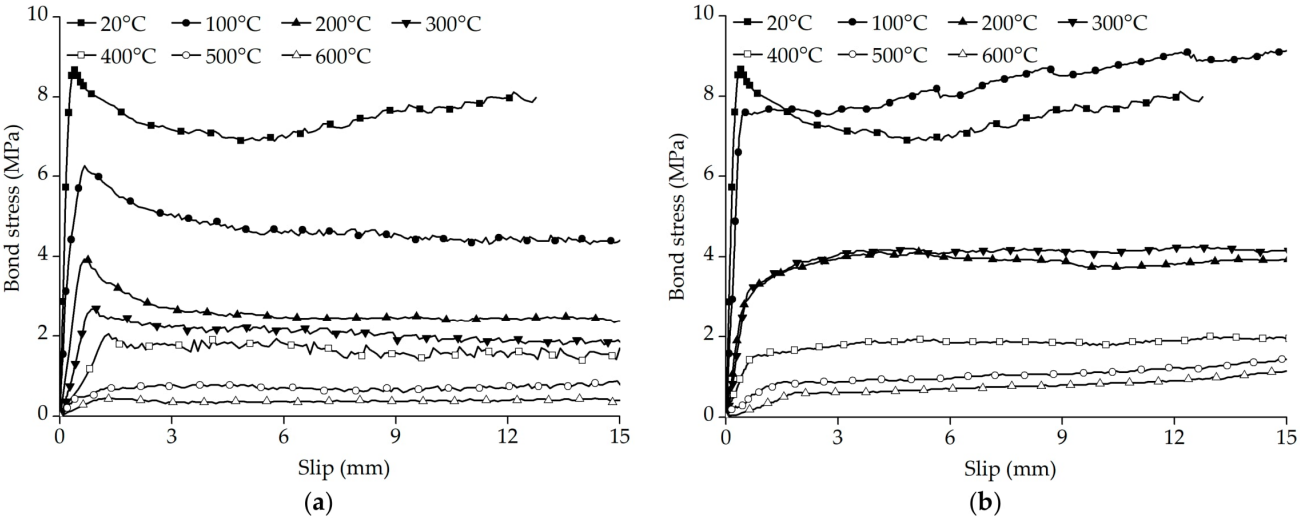

Figure 9. Bond–slip curves for mono-strand tendons: (**a**) at elevated temperatures; (**b**) after air cooling.

The initial rise in bond stress was approximately linear. A distinct bond–slip response after exposure to 100 °C was observed from the curves, as illustrated in Figure 9. This phenomenon may be associated with changes at the strand–grout interface during heating and cooling. Heating in this temperature range promotes water evaporation from

the cementitious grout, which would induce drying shrinkage and local microcracking, weaken the interfacial adhesion and alter the contact conditions. The resulting debonding or microcracking may persist after cooling, affecting the subsequent friction, mechanical interlock and bond behaviour. The subsequent increase may reflect the progressive mobilisation of friction and mechanical interlocking under the restraint retained by the grout–duct–concrete system. In specimens that underwent partial splitting while hot, this rise was followed by a reduction in stress and then an approximately constant residual resistance. The descending branch may have reflected concrete cracking and a loss of effective restraint. Friction at the interface may have become the principal source of resistance in the subsequent plateau [32].

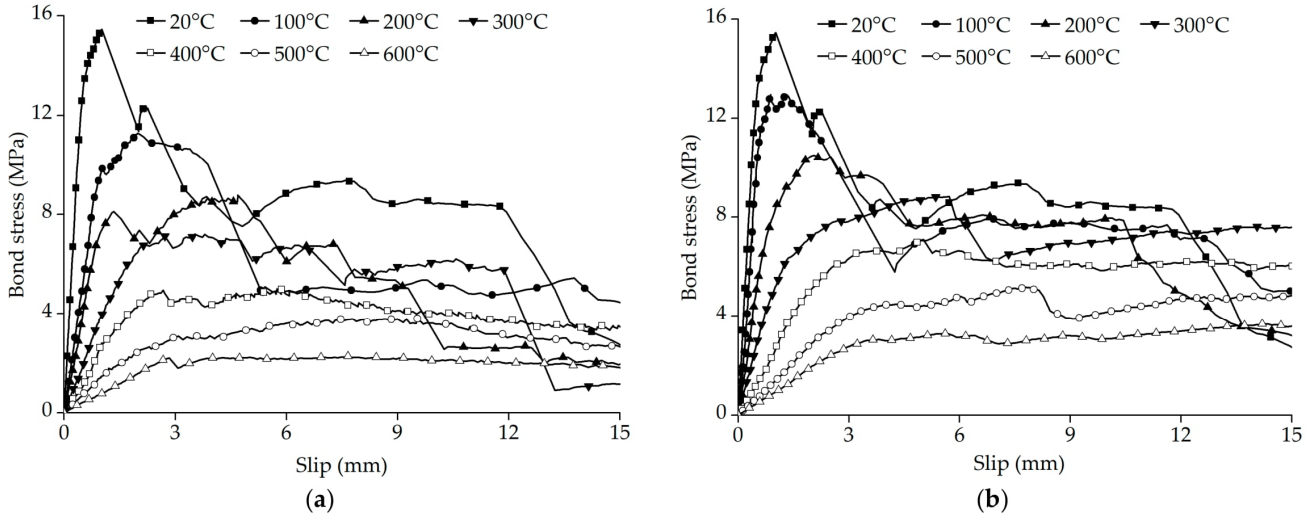

Figure 10. Bond–slip curves for triple-strand tendons: (**a**) at elevated temperatures; (**b**) after air cooling.

After air cooling, specimens with partial splitting exhibited a progressively decreasing tangent stiffness but no obvious reduction in bond stress after the initial rise. This response was consistent with continued restraint from the intact duct as damage developed in the grout and surrounding concrete. Recovery of steel properties after cooling [33] may have contributed to the retained duct restraint. This interpretation extrapolates the general behaviour of steel to the duct; neither its residual material properties nor the sequence of grout crushing was measured directly.

Through splitting was associated with a different response: bond stress dropped abruptly after the peak and approached a small residual value. Sectioning revealed a fractured corrugated duct in these specimens. The combination of brittle load loss and duct fracture was consistent with the importance of lateral restraint, although the post-test inspection alone could not establish the sequence of duct fracture and concrete splitting.

3.4. Effects of Water Cooling and Helical Confinement

For mono-strand tendons, the air-cooled curves in Figure 9b and the water-cooled curves in Figure 11a show similar bond responses over the conditions tested. The present comparison, therefore, indicated little influence of cooling method within this series. Studies of reinforcing-bar bond after heating provide related evidence on cooling effects [26,34], but their results concern different bond systems and do not extend the present observation to other tendon configurations or cooling procedures.

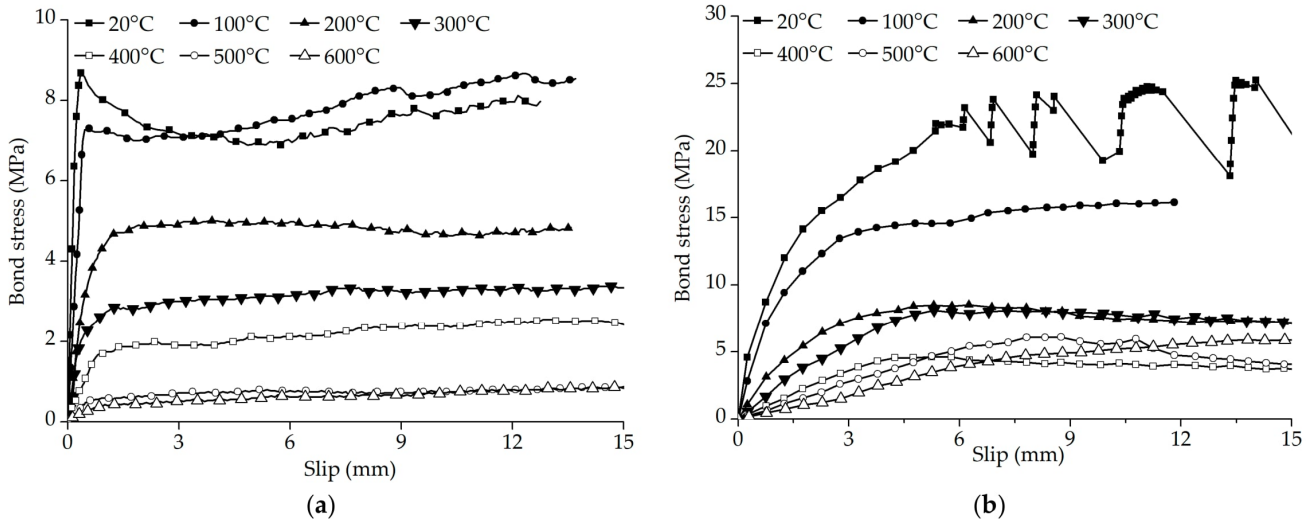

Figure 11. Bond–slip curves for tendons: (**a**) mono-strand specimens after water cooling; (**b**) triple-strand specimens with helical reinforcement.

The helically confined triple-strand specimens did not exhibit the abrupt post-peak stress drop seen in the corresponding specimens without helical reinforcement (Figures 10a and 11b). Their bond stress continued to increase with a gradually decreasing slope and showed no apparent reduction after the characteristic bond strength was reached. This behaviour suggested that the added reinforcement helped restrain the inner concrete during pull-out. Where the outer cover spalled, direct exposure of the helix to the furnace may have reduced its confinement contribution and contributed to the change in tangent stiffness.

4. Analytical Bond-Slip Model

The model was formulated by adapting the piecewise-linear framework used for centred grouted tendons [17] to the responses measured in the present eccentric configurations. Two features of these responses require attention when drawing on the fib model for reinforcing bars [35] or the strand model of Khalaf and Huang [2]. First, the measured initial branch was approximately linear, corresponding to a power-law exponent close to 1.0 rather than the commonly adopted value of 0.4. The dependence of initial bond stiffness on relative rib area in deformed bars [36] suggests, by analogy, that strand surface geometry may contribute to this difference. This is a mechanistic interpretation rather than direct verification for helical strands. Second, the present bond stresses were higher than those represented by these comparison models. Restraint supplied by the corrugated duct offers a possible explanation for this difference.

Three qualitative confinement levels were assigned from the post-peak branches in Figures 9–11 and the observed failure modes. These categories describe the measured response; they are not based on direct measurements of confining pressure.

Low confinement corresponds to through splitting and an abrupt loss of bond resistance, as observed for triple-strand specimens without additional helical reinforcement tested while hot at, or cooled from, temperatures not exceeding 300 °C. Medium confinement corresponds to partial splitting with a post-peak stress decrease; this category includes mono-strand specimens tested while hot and triple-strand specimens without helical reinforcement tested while hot above 300 °C. High confinement corresponds to partial splitting without an obvious post-peak decrease; it includes cooled mono-strand specimens, triple-strand specimens without helical reinforcement cooled from temperatures above 300 °C, and the helically reinforced triple-strand specimens. These categories were

inferred from the measured curves and observed failure modes, rather than from measurements of confining pressure. The lack of a quantitative relationship between confinement category, duct properties, transverse reinforcement, and the actual confinement pressure or transverse restraint is a limitation of the present model.

Figure 12 presents the resulting trilinear idealisation, which retains the characteristic-parameter approach of earlier bond models [2,17,35]. Its parameters are the characteristic bond strength t_{bmax}, initial bond stiffness E_b, ratio η of post-peak residual strength to characteristic bond strength, and characteristic slip s_1. Their values were obtained from the present test results. For the high-confinement response, η is 1.0 and the descending segment disappears, leaving a bilinear relation consisting of an ascending branch and a plateau; s_1 is then not needed to define a descending branch.

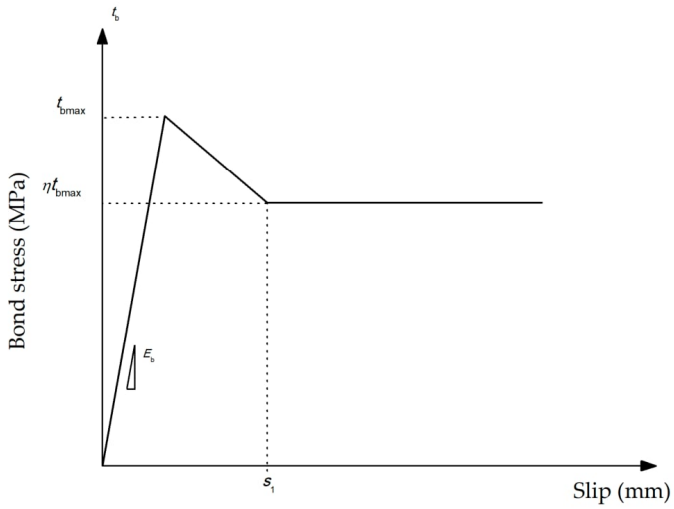

Figure 12. Analytical bond model for grouted tendons.

4.1. Initial Bond Stiffness

Initial bond stiffness is defined as the tangent slope at zero slip. The mean reference value E_b was 25 MPa/mm for both tendon configurations and was used as the ambient-temperature reference for normalisation. The stiffness evaluation and the regression in Equation (2) included a dataset of 53 specimens, covering all eccentricities, tests while hot and after cooling, water-cooled specimens and helically reinforced specimens. The initial stiffness $E_{b,T}$ was measured separately for each specimen under its test condition; Figure 13 shows these measured values normalised by E_b. In the thermal comparisons, T denotes the target temperature for tests while hot and the preceding peak exposure temperature for tests after cooling. Stiffness decreased markedly with temperature, while cooled specimens had somewhat higher values than specimens tested while hot at the corresponding temperature. Recovery of duct restraint after cooling is a possible contributor [33]. Equation (2) gives a common fit to the 53-specimen dataset, representing the overall temperature dependence without separately fitting this recovery:

$$E_{b,T}/E_b = 6.9\,(1 - 0.75T^{0.0445}),\ R^2 = 0.94. \quad (2)$$

The fitted relation is compared with the measurements in Figure 13. The coefficient of determination was $R^2 = 0.94$, indicating close agreement with the data used for the regression.

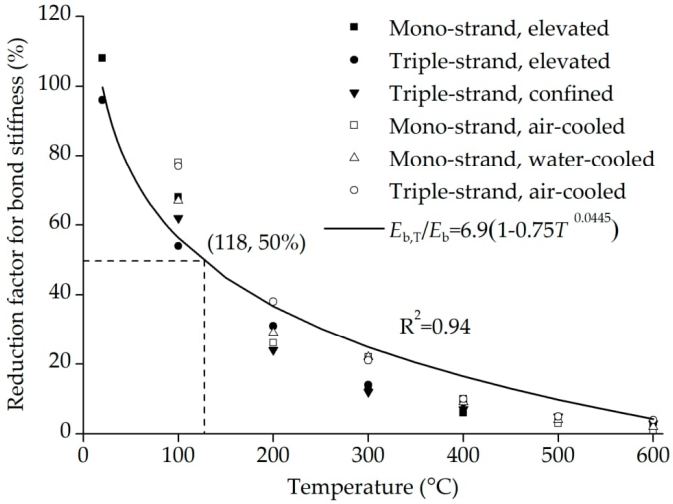

Figure 13. Regression for bond stiffness at various temperatures.

4.2. Bond Strength

4.2.1. Definition of Bond Strength

The ASTM procedure determines bond strength from the maximum measured pull-out load [18]. To compare curves with and without a distinct peak, the present study instead used a common characteristic-strength criterion. At ambient temperature, t_{bmax} is the bond stress at which the tangent stiffness falls to $0.1E_b$. For specimens tested while hot or after cooling, $t_{bmax,T}$ is the stress at which the tangent stiffness falls to $0.1E_{b,T}$, where $E_{b,T}$ is the initial stiffness corresponding to the relevant test condition. The same rule was applied to curves that approach a plateau without a clear peak. Consequently, the characteristic bond strength is not necessarily the highest stress recorded on the curve. This 10% criterion differs from the 20% initial-tangent-stiffness criterion used in the previous study [17], which should be considered when comparing characteristic strengths between the two programmes.

4.2.2. Bond Strength at Elevated Temperatures

Figure 14 shows decreasing characteristic bond strength with increasing exposure temperature for both tendon configurations, whether tested while hot or after cooling. The disproportionate loss near 100 °C reported in earlier work and associated with interfacial moisture loss [25] was not evident in the present tests. Cooling to ambient temperature produced a modest recovery in bond strength. For mono-strand specimens exposed to the same peak temperature, air and water cooling gave similar strengths.

Additional helical reinforcement increased ambient-temperature bond strength but had only a minor effect at 100–300 °C (Figure 14). In this range, spalling of the outer concrete cover exposed the helix directly to the furnace. Higher bond strengths were obtained with helical reinforcement at temperatures of 400 °C and above, where the outer cover remained intact in the tested specimens. The helix provides confinement to the lateral deformation of the inner concrete during splitting. Its resistance to deformation may increase the radial pressure on the duct through the concrete. Cover spalling changes the support at the helix and can increase the steel temperature, with a corresponding reduction in its mechanical properties. The remaining inner concrete and helix can provide resistance to further splitting. This is consistent with the retained post-peak resistance in Figure 11b, where the increase in characteristic strength was limited. The observations show that the confinement benefit varies with the condition of the cover; they do not establish a general temperature threshold for spalling.

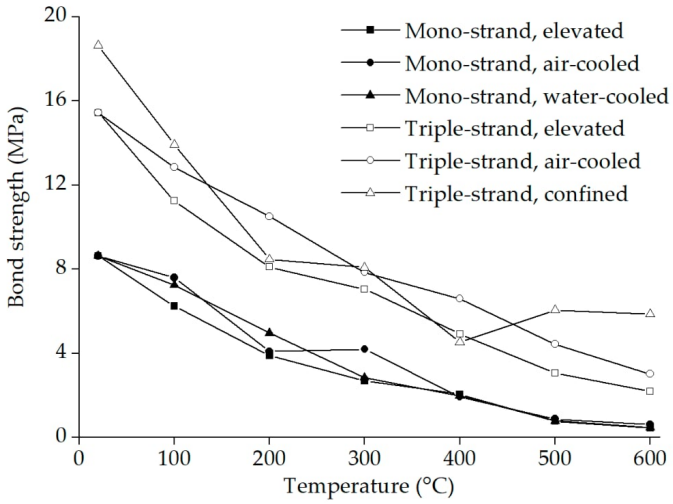

Figure 14. Bond strength at various temperatures.

At a given temperature, triple-strand tendons developed a higher equivalent bond strength than mono-strand tendons when evaluated using Equation (1) and the envelope perimeters in Figure 6. Their measured pull-out force was approximately four-times that of the mono-strand tendons at ambient temperature. Bundling, therefore, did not reduce the measured bond resistance in the configurations tested. This capacity benefit was accompanied by a greater tendency towards brittle splitting, so the strength advantage should be considered together with the post-peak response.

4.2.3. Ambient-Temperature Bond Strength and Its Empirical Representation

At maximum eccentricity, the average ambient-temperature bond strengths were 8.7 MPa for mono-strand tendons and 16.8 MPa for triple-strand tendons. The higher equivalent strength could be attributed to a combined effect of contact geometry, grout between strands and surrounding restraint. For the same pull-out force, the greater envelope perimeter gives a lower equivalent bond stress in Equation (1). The envelope represents an idealised failure surface, whereas the contacting strand surfaces and the grout between the strands determine the local force transfer. More contacting strand surface can increase the transferred force, but its contribution cannot be obtained from the envelope perimeter alone. The surrounding grout, duct and concrete restrain lateral deformation and provide the support needed for friction and mechanical interlocking to develop. The through splitting and duct fracture observed in triple-strand specimens without helical reinforcement show the importance of the surrounding material and duct in limiting this resistance. The combined effect is complicated, and the individual contribution of each effect could not be distinguished since their contributions were not measured separately in these tests. For comparison, the local bond–slip model in the fib Model Code [35] was used as a reference for conventional ribbed reinforcing bars under monotonic loading before steel yielding. The selected case was splitting failure under good bond conditions with stirrup confinement. The tabulated splitting parameters correspond to bar diameters $\varphi \leq 20$ mm, $c_{min} = \varphi$, $c_{max}/c_{min} = 2$ and a transverse reinforcement index $K_{tr} = 0.02$ for the stirrup-confined case, where c_{min} and c_{max} describe the effective cover and spacing conditions. These conditions define the reinforcing-bar benchmark; they were not assumed to be satisfied by the grouted-strand specimens. The corresponding simplified strength expression was written in the notation of the present study as follows:

$$t_{bmax} = 8.0\ (f_c/25)^{0.25}, \quad (3)$$

where f_c is the compressive strength of the embedding material. The reference framework concerns ordinary reinforcing bars in concrete; in the present comparison, a rounded reference grout strength of 40 MPa was substituted for the embedding-material strength. Equation (3) then gives 9.0 MPa for comparison with the mono-strand result. In Equations (3) and (4), t_{bmax} denotes the characteristic bond strength.

The higher strength of the triple-strand configuration is consistent with the size dependence reported for reinforcing bars at a given confinement level [37], although the present data do not establish a general size law. In particular, they are insufficient to identify separate effects of tendon diameter and transverse reinforcement. An approximate expression was, therefore, adopted using the equivalent tendon diameter $d_{b,e} = l_e/\pi$, where l_e is the envelope perimeter in Figure 6. Following the strength dependence in Equation (3), bond strength was assumed proportional to $d_{b,e}(f_c/25)^{0.25}$. Regression of the available results yielded a proportionality coefficient of 0.5, with $d_{b,e}$ expressed in mm and both f_c and t_{bmax} in MPa:

$$t_{bmax} = 0.5\ d_{b,e}\ (f_c/25)^{0.25}. \quad (4)$$

For the triple-strand configuration, substitution of d_b = 15.2 mm, $d_{b,e} = (\pi + 3)d_b/\pi$ and f_c = 40 MPa into Equation (4) gives 16.71 MPa, slightly below the measured mean of 16.8 MPa at maximum eccentricity. As the present experimental results were used in developing Equation (4), this comparison is, therefore, regarded as an illustration of acceptable agreement.

4.2.4. Regression for Bond Strength at Elevated Temperatures

Temperature-dependent bond relationships have been developed for bars and strands [2,20,34]. Other studies consider bond deterioration together with changes in the surrounding material [38,39], while Yu and Kodur [40] address a different interface involving near-surface-mounted FRP reinforcement. For the present grouted tendons, the measured resistance depends on the grout as well as restraint from the duct and surrounding concrete. A relation based only on grout compressive strength would, therefore, omit other contributions. The bond-strength reduction factor was fitted directly against temperature for the mono- and triple-strand results using the following power relation:

$$t_{bmax,T}/t_{bmax} = 1.25 - 0.06\ T^{0.46}. \quad (5)$$

Figure 15 compares the fitted reduction factor with the experimental results. The regression yielded R^2 = 0.93, indicating close agreement with the calibration data. The variation in the bond stiffness and bond strength, as illustrated in Figures 13 and 15, shows that the fitted temperature corresponding to approximately 50% reduction in initial stiffness is about 118 °C, whereas the corresponding temperature for bond strength is approximately 242 °C. This difference could be attributed to the local cracking and loss of contact, which play a significant role in reducing the initial slope at small slip, while friction and the remaining duct restraint can still provide resistance for the bond strength with increasing slip.

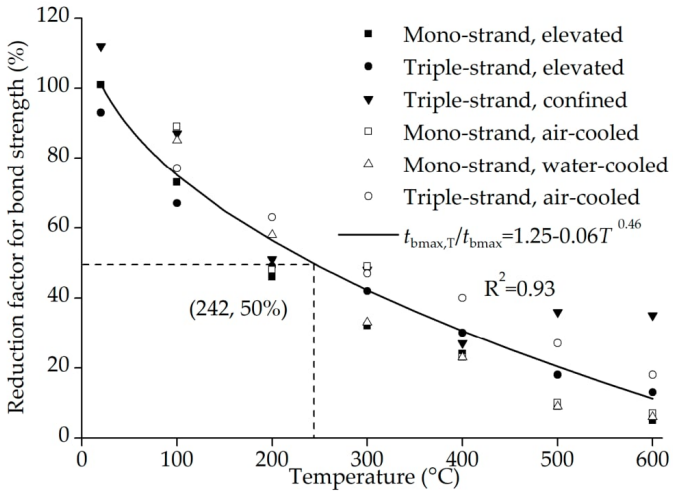

Figure 15. Regression for bond strength at various temperatures.

4.3. Post-Peak Residual Strength and Characteristic Slip

The residual resistance considered here is the post-peak bond resistance, distinct from bond strength measured after thermal exposure and cooling. Its value $t_{bf,T}$ was normalised by the corresponding characteristic bond strength to give η. Through splitting under low confinement left negligible resistance, represented by η = 0. Under medium confinement, a descending branch led to a residual plateau; the ratios in Figure 16 averaged approximately 0.7. For the stirrup-confined splitting case in the fib local bond–slip model [35], the residual-to-splitting strength ratio is 0.4. The measured mean of approximately 0.7 was, therefore, about 1.75-times. This comparison concerns model ratios for different reinforcement systems and strength definitions. Under high confinement, the absence of an evident post-peak reduction is represented by η = 1.0.

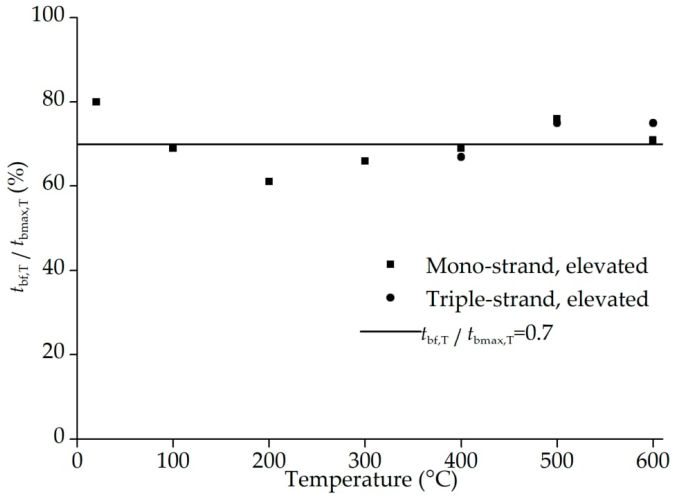

Figure 16. Post-peak residual-to-characteristic bond strength ratio at various temperatures.

For low and medium confinement, the model replaces the descending response with a straight segment joining the characteristic bond strength to the residual plateau (Figure 12). The reference point for extracting this segment was the characteristic-strength point defined by the 10% tangent stiffness, rather than necessarily the actual maximum of the experimental curve. A second point was selected on the subsequent descending branch where the secant slope is 0.1 of the secant slope evaluated at the characteristic-strength point. Thus, the slopes used in this extraction step are secant slopes, distinct from the tangent stiffness used to define characteristic strength. The intersection of the resulting descending segment

with the residual plateau defines s_1. Figure 17 indicates little variation in this characteristic slip with temperature. The average values were 2.5 mm for mono-strand tendons and 5.1 mm for triple-strand tendons. These values were approximated by $d_{b,e}/6$, which gives 2.53 mm and 4.95 mm, respectively.

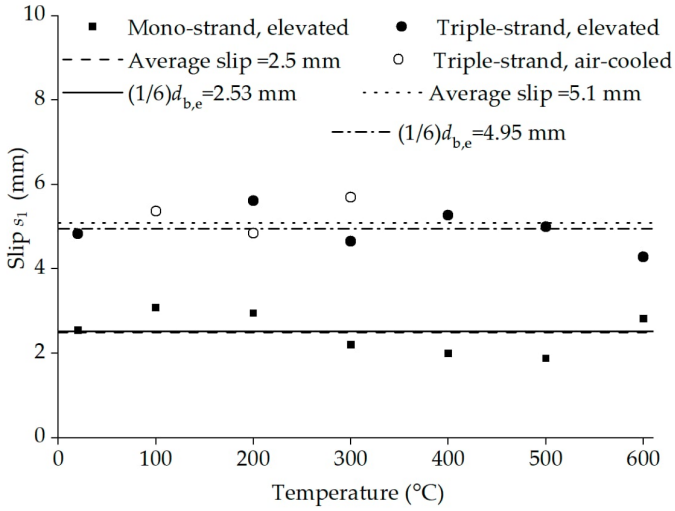

Figure 17. Characteristic slip s_1 for mono- and triple-strand tendons at various temperatures.

4.4. Summary and Scope of the Model Parameters

Table 3 summarises the parameter expressions for the bond–slip model over 20–600 °C. Their calibration concerned the tested mono- and triple-strand arrangements, with the heated series at maximum eccentricity. A confinement category is required to select the post-peak response. Because these categories were inferred from measured bond–slip curves and failure modes, and no relationship with confining pressure or transverse reinforcement ratio was established, their assignment before testing remains a limitation. The fitted relations describe the calibration data and do not constitute independent validation for other tendon sizes, duct geometries, eccentricities or heating histories. The tests also did not quantify the influence of initial prestress, as none was applied. Independent validation using data not involved in model development was not performed. The predictive capability of Equation (4) beyond the tested configurations, therefore, remains to be established. To illustrate the application of the proposed bond-slip relationship in structural fire engineering, a prestressed concrete bridge girder under hydrocarbon fire was modeled, as shown in Appendix B.

Table 3. Parameters of the bond–slip relationship over 20–600 °C.

Parameter	Value
t_{bmax} (MPa)	$0.5\, d_{b,e}\, (f_c/25)^{0.25}$
$t_{bmax,T}$ (MPa)	$(1.25 - 0.06\, T^{0.46})\, t_{bmax}$
$t_{bf,T}$ (MPa)	η [1] $t_{bmax,T}$
s_1 (mm)	$(1/6)\, d_{b,e}$
$E_{b,T}$ (MPa/mm)	$172.5\, (1 - 0.75T^{0.0445})$

[1] η = 0, 0.7 and 1.0 for low, medium and high confinement, respectively.

The mechanical properties of prestressing steel also affect the response of bonded post-tensioned members during heating and after cooling. The reduction in steel yield strength during heating allows yielding at a lower tendon force [23,29]. Zhang et al. [23] reported that BS 5896 steel retained approximately its original tensile strength after cooling from 300 °C. At this temperature, the present air-cooled mono- and triple-strand specimens

retained around half of their ambient bond strengths. Bond degradation, therefore, remains significant even where steel strength largely recovers. Reductions in steel stiffness, together with high-temperature creep and stress relaxation, may reduce the effective prestressing force. Recovery of steel strength or stiffness after cooling does not necessarily restore the initial prestressing force because irreversible deformation and interfacial slip may remain. Bond degradation and steel deterioration, therefore, need to be considered jointly through force equilibrium and deformation compatibility when assessing member performance.

5. Conclusions

Fifty-three pull-out tests investigated tendon eccentricity at ambient temperature and the response of grouted tendons at maximum eccentricity during heating and after cooling. This study shows that increasing eccentricity reduced ambient-temperature bond strength without substantially changing the bond–slip curve shape. The thermal response at intermediate eccentricities was not established. Bond strength and initial stiffness decreased with temperature. The fitted relationships indicated approximately 50% losses at 242 °C and 118 °C, respectively. Medium-confinement specimens retained approximately 70% of their characteristic strength on average after the post-peak decline. High-confinement specimens showed little reduction, whereas through splitting with duct fracture left negligible residual resistance. Triple-strand tendons developed greater bond resistance than mono-strand tendons but were more susceptible to brittle splitting. Cooling produced modest strength recovery. Air cooling and water spraying yielded similar bond responses for the tested mono-strand specimens. Helical reinforcement improved bond behaviour, although its strength contribution during heating depended on concrete cover integrity. Spalling may have reduced its confinement effectiveness. A trilinear bond–slip model was calibrated for the three observed confinement categories, reducing to a bilinear model under high confinement. Broader application requires further assessment, including determination of confinement categories independently of measured bond–slip curves.

Author Contributions: Conceptualization, F.T.K.A.; methodology, X.W.; formal analysis, X.W.; investigation, X.W.; writing—original draft preparation, X.W. and C.R.; writing—review and editing, X.W., C.R., T.H. and W.X.; supervision, F.T.K.A.; funding acquisition, X.W. and W.X. All authors have read and agreed to the published version of the manuscript.

Funding: This work was funded by the National Key R&D Program of China, grant number 2024YFE0216700, and the National Natural Science Foundation of China, grant number 52108480.

Data Availability Statement: Data are contained within the article.

Conflicts of Interest: The authors declare no conflicts of interest.

Abbreviations

d_b	Strand diameter
$d_{b,e}$	Equivalent tendon diameter based on the envelope perimeter
E_b	Reference initial bond stiffness at ambient temperature
$E_{b,T}$	Initial bond stiffness associated with exposure temperature T
f_c	Compressive strength of the embedding material (cement grout in this study)
l_b	Bonded length
l_e	Tendon envelope perimeter
P	Pull-out force
s_1	Slip at the onset of the idealised post-peak residual plateau
t_b	Bond stress

$t_{bf,T}$	Post-peak residual bond strength associated with exposure temperature T
t_{bmax}	Characteristic bond strength at ambient temperature
$t_{bmax,T}$	Characteristic bond strength associated with exposure temperature T
η	Ratio of post-peak residual strength to characteristic bond strength

Appendix A. Illustration of Test Data

Appendix A.1. Tested Strength of the Specimen

Table A1 lists the characteristic bond strengths of the pull-out specimens, the mean compressive strengths of the grout and concrete cylinders, and the measured ultimate tensile strength of the strands. It should be noted that the ultimate tensile strength of the strand tendon was tested once instead of each test series considering that the performance of the same batch of strand tendons may not vary significantly. The specimen designation consists of four components separated by hyphens. The first component indicates the number of steel strands, with "1" and "3" denoting specimens containing one and three strands, respectively. The second component specifies the eccentricity in millimetres; for example, "8.6" represents an eccentricity of 8.6 mm. The third component denotes the prescribed maximum exposure temperature in degrees Celsius, with "20" indicating ambient-temperature testing and "100" indicating a prescribed maximum exposure temperature of 100 °C. The final component identifies the replicate number, testing condition, or reinforcement configuration. The numerical suffixes "1" and "2" distinguish the first and second replicate specimens, respectively, tested at ambient temperature under otherwise-identical conditions. For the letter suffixes, "Amb" denotes testing at ambient temperature; "Air" and "Water" denote testing after exposure to the prescribed maximum temperature followed by air cooling and water cooling, respectively; "Hot" denotes testing at the prescribed maximum temperature; and "Con" indicates the presence of helical reinforcement to provide confinement in the specimen.

Table A1. Tested strength of the specimens.

Test Series	Specimen	Bond Strength (MPa)	Mean Grout Strength (MPa)	Mean Concrete Strength (MPa)	Mean Tendon Strength (MPa)
1	1-0-20-1	11.95	43.4	49.9	1910
1	1-0-20-2	11.63			
1	1-4.8-20-1	11.09			
1	1-4.8-20-2	11.42			
1	1-8.8-20-1	12.04			
1	1-8.8-20-2	10.38			
1	1-12.8-20-1	12.01			
1	1-12.8-20-2	10.33			
1	1-16.4-20-1	8.56			
1	1-16.4-20-2	8.83			
1	3-0-20-1	17.89			
1	3-0-20-2	17.60			
1	3-4.6-20-1	17.95			
1	3-4.6-20-2	17.22			
1	3-8.6-20-1	16.81			
1	3-8.6-20-2	15.61			

Table A1. *Cont.*

Test Series	Specimen	Bond Strength (MPa)	Mean Grout Strength (MPa)	Mean Concrete Strength (MPa)	Mean Tendon Strength (MPa)
2	1-16.4-100-Hot	6.26			
2	1-16.4-200-Hot	3.91			
2	1-16.4-300-Hot	2.70			
2	1-16.4-400-Hot	2.06			
2	1-16.4-500-Hot	0.78			
2	1-16.4-600-Hot	0.45	41.5	51.8	
2	1-16.4-100-Air	7.60			
2	1-16.4-200-Air	4.09			
2	1-16.4-300-Air	4.20			
2	1-16.4-400-Air	1.93			
2	1-16.4-500-Air	0.88			
2	1-16.4-600-Air	0.62			
3	3-8.6-100-Hot	11.25			
3	3-8.6-200-Hot	8.11			
3	3-8.6-300-Hot	7.05			
3	3-8.6-400-Hot	4.94			
3	3-8.6-500-Hot	3.07			
3	3-8.6-600-Hot	2.18			
3	3-8.6-100-Air	12.86	41.2	47.4	1910
3	3-8.6-200-Air	10.51			
3	3-8.6-300-Air	7.86			
3	3-8.6-400-Air	6.60			
3	3-8.6-500-Air	4.45			
3	3-8.6-600-Air	3.02			
4	1-16.4-100-Water	7.25			
4	1-16.4-200-Water	4.98			
4	1-16.4-300-Water	2.85			
4	1-16.4-400-Water	1.98	41.0	51.8	
4	1-16.4-500-Water	0.80			
4	1-16.4-600-Water	0.48			
5	3-8.6-20-Con	18.64			
5	3-8.6-100-Con	13.93			
5	3-8.6-200-Con	8.48			
5	3-8.6-300-Con	8.09	43.9	48.1	
5	3-8.6-400-Con	4.54			
5	3-8.6-500-Con	6.06			
5	3-8.6-600-Con	5.88			

Appendix A.2. Tendon Eccentricity

Figure A1 shows a schematic illustration of the grout-thickness distribution for different eccentricities, taking the mono-strand specimens as an example. The shorter path on the thin side can develop local bearing early in the pull-out response. The radial-gap varies with the angle from the eccentricity direction, as illustrated in Figure A1b. The effective internal geometry was defined such that the mono-strand tendon contacts the duct at an eccentricity of 16.4 mm. The radial grout thickness on the near and far sides are then 16.4 minus the eccentricity and 16.4 plus the eccentricity, respectively. At eccentricities of 0, 4.8, 8.8, 12.8 and 16.4 mm, the corresponding near-side thicknesses are 16.4, 11.6, 7.6, 3.6 and 0 mm.

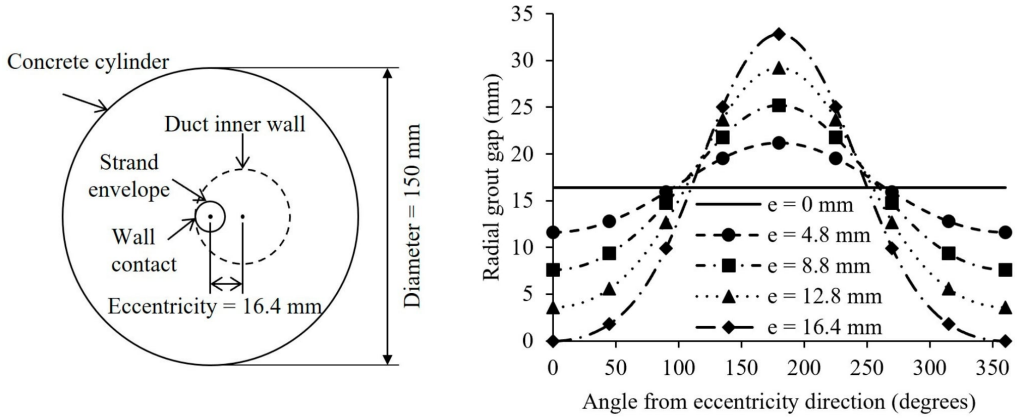

Figure A1. Schematic illustration of the grout-thickness distribution for different eccentricities: (**a**) eccentric grout geometry; (**b**) analytical radial-gap distribution.

Appendix B. Application of the Proposed Bond–Slip Model

To illustrate application of the proposed bond–slip model in structural fire engineering, post-tensioned concrete girder specimens F1 and F2 under hydrocarbon fire studied by Wu et al. [41], were modelled (Figure A2). A quarter of the girder was modelled considering symmetry. Concrete, grout and the equivalent solid tendon were modelled using C3D8R elements. A layer of cohesive element COH3D8 was modelled to connect the tendon and grout elements, as adopted in the study by Wu et al. [41]. Two simulations were conducted for comparison with one simulation using temperature-independent bond properties at 20 °C and the other simulation using the maximum-eccentricity bond relationship in Table 3 with a triple-strand envelope. The bond–slip model was defined in the in-plane directions as a type of traction–separation relationship, as illustrated in Figure A2b. All the other settings of the models were the same as those conducted by Wu et al. [41].

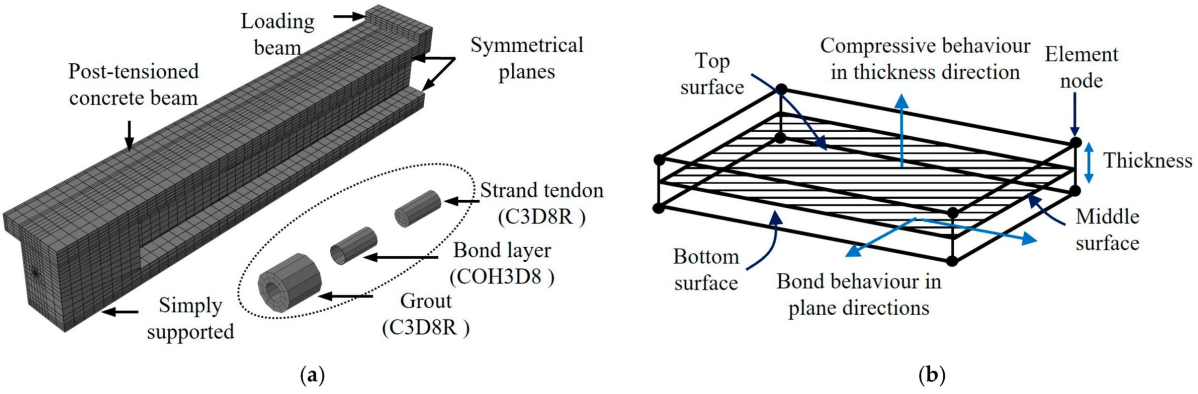

Figure A2. Finite-element mesh: (**a**) quarter box-girder model; (**b**) bond–slip model definition method in the in-plane directions for traction–separation relationship on a cohesive element COH3D8.

After self-weight and prestressing were applied, the girder was loaded to 160 kN and heated for either 90 min (Specimen F2) or 180 min (Specimen F1) using the hydrocarbon-fire temperature field. Specimen F2 was then left to be cooled down while keeping the sustained load unchanged. Local slip was the longitudinal relative displacement of opposing tendon and grout nodes, measured from bond activation. Mean absolute slip was calculated over 416 node pairs. The downward midspan displacement during reloading was measured from the after-cooling state. The total load refers to the full girder. Values at common loads are interpolated between adjacent output frames. The calculated tendon temperatures

ranged from 117.1 to 182.0 °C after 90 min and from 217.2 to 417.5 °C after 180 min. The temperature distribution along the curved tendon gave different local bond properties. The application used the local temperature history to assign these properties.

After 180 min under 160 kN, the temperature-dependent and 20 °C bond calculations gave maximum absolute local slips of 0.1400 and 0.1052 mm, respectively, as illustrated in Figure A3a. The larger local slip of the simulation adopting the temperature-dependent bond–slip model could be attributed to the degradation of the bond properties at elevated temperatures. Figure A3b shows the bond stress denoted as longitudinal interface traction after cooling down from a 90 min fire exposure. The bond stress was larger for the simulation adopting the temperature-dependent bond–slip model, meaning that the stress could be underestimated if the high-temperature deterioration of the bonding performance was ignored. Following cooling of Specimen F2 under the sustained load of 160 kN, the tendon axial forces ranged from 173.2 to 266.6 kN for the temperature-dependent bond model and from 168.8 to 269.0 kN for the model retaining the ambient-temperature bond properties, as shown in Figure A3c. Thus, within the adopted model and loading conditions, deterioration of the bond relationship does not cause an immediate loss of tendon force after cooling. The result is consistent with continued force transfer through the available interface resistance and end anchorage. At the member level, residual contact resistance and bond in less-damaged regions may sustain structural interaction despite local slip. The measured equivalent bond relationship represents the combined response of the tested grouted-tendon system. Local bond reduction factors alone cannot determine the reduction in member capacity, which also depends on the extent and location of damage, residual prestress, material deterioration and anchorage integrity. Eccentricity within a duct changes the local grout thickness, whereas the tendon position within the member also affects its thermal exposure. These effects should be distinguished when transferring the measured bond relationship to a structural member.

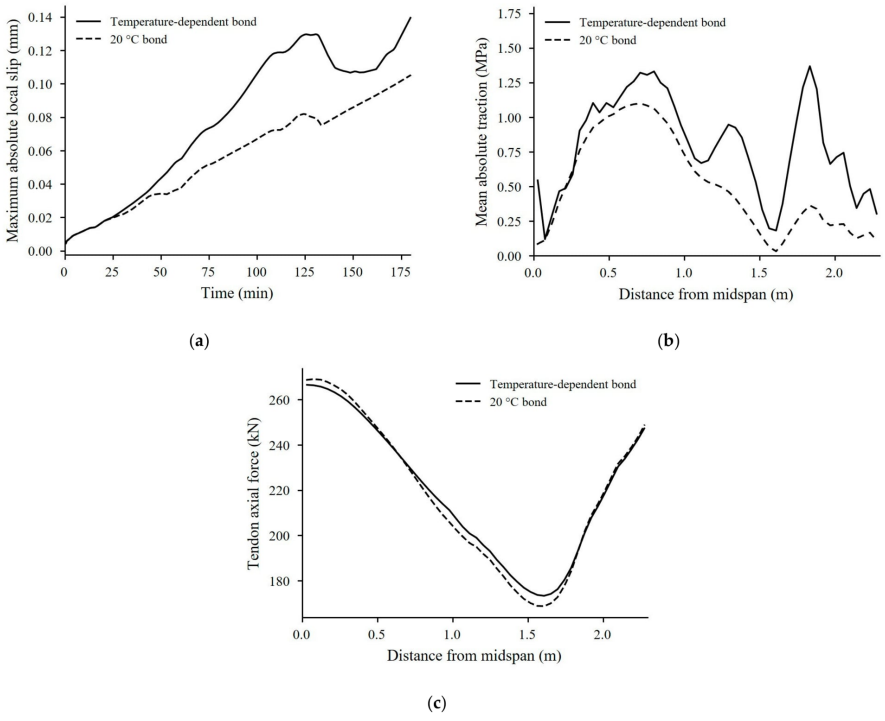

Figure A3. Bond response and tendon axial-force distribution: (**a**) maximum absolute local slip after heating for 180 min for Specimen F1; (**b**) mean absolute longitudinal traction of cohesive elements after cooling down for Specimen F2; (**c**) the axial force along the tendon after cooling down for Specimen F2.

References

1. Jeyashree, T.M.; Kannan Rajkumar, P.R.; Satyanarayanan, K.S. Developments and research on fire response behaviour of prestressed concrete members—A review. *J. Build. Eng.* **2022**, *57*, 104797. [CrossRef]
2. Khalaf, J.; Huang, Z. Analysis of the bond behaviour between prestressed strands and concrete in fire. *Constr. Build. Mater.* **2016**, *128*, 12–23. [CrossRef]
3. Abrishami, H.G.; Mitchell, D. Bond Characteristics of Pretensioned Strand. *ACI Mater. J.* **1993**, *90*, 228–235. [CrossRef] [PubMed]
4. Dai, L.; Tao, Y.; Yuan, P.; Wang, L. 3D meso-scale modeling of bond behavior between helical strand and concrete. *Eng. Struct.* **2024**, *309*, 118041. [CrossRef]
5. Ferretti, D.; Pagliari, F.; Belletti, B. Bond of post-tensioning strands in case of grouting defects. *Constr. Build. Mater.* **2024**, *426*, 136133. [CrossRef]
6. Asghari Ghajari, F.; Yousefpour, H. Residual bond-slip behavior in reinforced concrete members exposed to elevated temperatures. *Struct. Concr.* **2023**, *24*, 3281–3298. [CrossRef]
7. Das, A.; Bošnjak, J.; Sharma, A. Post-fire bond behaviour of reinforcement in concrete considering different bonded lengths and position of rebars. *Eng. Struct.* **2023**, *296*, 116908. [CrossRef]
8. Bošnjak, J.; Das, A.; Sharma, A. Influence of concrete cover and transverse reinforcement on residual post-fire bond performance of reinforcement in concrete. *Eng. Struct.* **2024**, *314*, 118191. [CrossRef]
9. Liu, L.; Ouyang, X.; Wang, X.; Zhang, Q. Multi-factors effects on developments of bond behaviors between the high-strength grout and steel rebar and its optimization. *Structures* **2025**, *77*, 109067. [CrossRef]
10. Liu, L.; Sun, W.; Xiao, J.; Li, W.; Jian, L.; Zhang, Q. Bond behavior between high-strength grout and rebar after exposure to elevated temperatures. *Structures* **2024**, *69*, 107308. [CrossRef]
11. Xiao, J.; Li, Z.; Xie, Q.; Shen, L. Effect of strain rate on compressive behaviour of high-strength concrete after exposure to elevated temperatures. *Fire Saf. J.* **2016**, *83*, 25–37. [CrossRef]
12. Xiao, J.; Xie, Q.; Xie, W. Study on high-performance concrete at high temperatures in China (2004–2016)—An updated overview. *Fire Saf. J.* **2018**, *95*, 11–24. [CrossRef]
13. Liu, C.; Zheng, J.; Ning, N.; Yan, L.; Zheng, C. Experimental study of bond performance of corroded reinforcement in concrete under various cooling methods. *J. Build. Eng.* **2024**, *84*, 108569. [CrossRef]
14. Abuhishmeh, K.; Jalali, H.H.; Ebrahimi, M.; Soltanianfard, M.A.; Correa, C.O.; Cornejo, J.S. Behavior of high strength reinforcing steel rebars after high temperature exposure: Tensile properties and bond behavior using pull-out and end beam tests. *Eng. Struct.* **2024**, *305*, 117730. [CrossRef]
15. Peng, T.; Miao, J.; Song, B.; Liu, Y.; Zhang, J.; Sun, D.; Song, S. Experimental study on bonding performance of steel rebar and grout at different positions after elevated temperatures. *Appl. Sci.* **2026**, *16*, 1053. [CrossRef]
16. Li, M.R.; Wang, T.C.; Liang, J.; Teng, N.G.; Gao, W.Y. Local bond-slip model between steel bars and concrete after exposure to high temperatures. *Adv. Struct. Eng.* **2025**, *28*, 1440–1460. [CrossRef]
17. Wu, X.Q.; Huang, T.; Zhang, L.; Au, F.T.K. Bond performance of grouted tendons at elevated temperatures. *Proc. Inst. Civ. Eng. Struct. Build.* **2021**, *174*, 791–803. [CrossRef]
18. *ASTM A1081/A1081M-12*; Standard Test Method for Evaluating Bond of Seven-Wire Steel Prestressing Strand. ASTM International: West Conshohocken, PA, USA, 2012. [CrossRef]
19. RILEM/CEB/FIP. *RC6: Bond Test for Reinforcement Steel. 2: Pull-Out Test*; CEB News 73; CEB: Lausanne, Switzerland, 1983.
20. Aslani, F.; Samali, B. Predicting the bond between concrete and reinforcing steel at elevated temperatures. *Struct. Eng. Mech.* **2013**, *48*, 643–660. [CrossRef]
21. Diederichs, U.; Schneider, U. Bond strength at high temperatures. *Mag. Concr. Res.* **1981**, *33*, 75–84. [CrossRef]
22. *BS 5896:2012*; High Tensile Steel Wire and Strand for the Prestressing of Concrete—Specification. BSI: London, UK, 2012. [CrossRef]
23. Zhang, L.; Wei, Y.; Au, F.T.K.; Li, J. Mechanical properties of prestressing steel in and after fire. *Mag. Concr. Res.* **2017**, *69*, 379–388. [CrossRef]
24. Hertz, K. The anchorage capacity of reinforcing bars at normal and high temperatures. *Mag. Concr. Res.* **1982**, *34*, 213–220. [CrossRef]
25. Royles, R.; Morley, P.D. Further responses of the bond in reinforced concrete to high temperatures. *Mag. Concr. Res.* **1983**, *35*, 157–163. [CrossRef]
26. Ahmed, A.E.; Al-Shaikh, A.H.; Arafat, T.I. Residual compressive and bond strengths of limestone aggregate concrete subjected to elevated temperatures. *Mag. Concr. Res.* **1992**, *44*, 117–125. [CrossRef]
27. Pinoteau, N.; Pimienta, P.; Guillet, T.; Rivillon, P.; Rémond, S. Effect of heating rate on bond failure of rebars into concrete using polymer adhesives to simulate exposure to fire. *Int. J. Adhes. Adhes.* **2011**, *31*, 851–861. [CrossRef]
28. *EN 1991-1-2:2002*; Eurocode 1: Actions on Structures—Part 1-2: General Actions—Actions on Structures Exposed to Fire. CEN: Brussels, Belgium, 2002.

29. *EN 1992-1-2:2004*; Eurocode 2: Design of Concrete Structures—Part 1-2: General Rules—Structural Fire Design. CEN: Brussels, Belgium, 2004.
30. *EN 1993-1-2:2005*; Eurocode 3: Design of Steel Structures—Part 1-2: General Rules—Structural Fire Design. CEN: Brussels, Belgium, 2005.
31. ACI Committee 408. *ACI 408R-03: Bond and Development of Straight Reinforcing Bars in Tension*; American Concrete Institute: Farmington Hills, MI, USA, 2003.
32. Eligehausen, R.; Popov, E.P.; Bertero, V.V. *Local Bond Stress-Slip Relationships of Deformed Bars under Generalized Excitations: Experimental Results and Analytical Model*; Report UCB/EERC-83/23; Earthquake Engineering Research Center, University of California: Berkeley, CA, USA, 1983.
33. *EN 1994-1-2:2005*; Eurocode 4: Design of Composite Steel and Concrete Structures—Part 1–2: General Rules—Structural Fire Design. CEN: Brussels, Belgium, 2005.
34. Bingöl, A.F.; Gül, R. Residual bond strength between steel bars and concrete after elevated temperatures. *Fire Saf. J.* **2009**, *44*, 854–859. [CrossRef]
35. fib. *fib Model Code for Concrete Structures 2010*; Ernst & Sohn: Berlin, Germany, 2013. [CrossRef]
36. Darwin, D.; Graham, E.K. Effect of deformation height and spacing on bond strength of reinforcing bars. *ACI Struct. J.* **1993**, *90*, 646–657. [CrossRef] [PubMed]
37. Zuo, J.; Darwin, D. *Bond Strength of High Relative Rib Area Reinforcing Bars*; Structural Engineering and Engineering Materials Report No. 46; University of Kansas Center for Research, Inc.: Lawrence, KS, USA, 1998.
38. Haddad, R.H.; Shannis, L.G. Post-fire behavior of bond between high strength pozzolanic concrete and reinforcing steel. *Constr. Build. Mater.* **2004**, *18*, 425–435. [CrossRef]
39. Haddad, R.H.; Al-Saleh, R.J.; Al-Akhras, N.M. Effect of elevated temperature on bond between steel reinforcement and fiber reinforced concrete. *Fire Saf. J.* **2008**, *43*, 334–343. [CrossRef]
40. Yu, B.; Kodur, V.K.R. Effect of high temperature on bond strength of near-surface mounted FRP reinforcement. *Compos. Struct.* **2014**, *110*, 88–97. [CrossRef]
41. Wu, X.Q.; Huang, T.; Au, F.T.K.; Li, J. Posttensioned Concrete Bridge Beams Exposed to Hydrocarbon Fire. *J. Struct. Eng.* **2020**, *146*, 04020210. [CrossRef]

Disclaimer/Publisher's Note: The statements, opinions and data contained in all publications are solely those of the individual author(s) and contributor(s) and not of MDPI and/or the editor(s). MDPI and/or the editor(s) disclaim responsibility for any injury to people or property resulting from any ideas, methods, instructions or products referred to in the content.